Chemical Engineering & Processing: Process Intensification 204 (2024) 109930

Contents lists available at ScienceDirect

Chemical Engineering and Processing - Process Intensification

journal homepage: www.elsevier.com/locate/cep

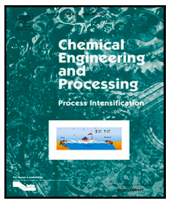

Conceptual study on the intensification of gas–liquid mass transfer in trickle bed reactors by the application of strut-based and novel sheet-based periodic open cellular structures (POCS)

Hendrik Held, Hannsjörg Freund *

Technische Universität Dortmund, Lehrstuhl Reaction Engineering and Catalysis, Emil-Figge-Str. 66, 44227, Dortmund, Germany

ARTICLE INFO

Keywords:
Gas–liquid mass transfer
Pressure drop
Trickle bed reactor
Process intensification
Structured catalyst
POCS
Meander flow

ABSTRACT

Rapid progress in the development of additive manufacturing technology enables the production of structured reactor internals of complex geometry. To address mass transport limitations structured internals can be used in trickle bed reactors (TBRs) as the most frequently used reactor for heterogeneously catalyzed multiphase reactions. However, reactions in TBRs are frequently limited by gas–liquid mass transfer.

As periodic open cellular structures (POCS) as reactor internals were not addressed regarding g–l mass transfer yet, this contribution provides first data on gas–liquid mass transfer for different types of POCS. Therefore, desorption of dissolved oxygen in water with nitrogen gas and the two-phase pressure drop were measured. Strut-based Kelvin and diamond unit cell POCS were compared to a sphere random packed bed as a benchmark. A novel sheet-based unit cell was developed realizing meandering channels demonstrating a fivefold increase in volumetric mass transfer coefficient compared to the benchmark. To compare the performance of the setup with literature data, state of the art neural network correlations were used for comparison. This proof of concept highlights the potential of additively manufactured POCS for intensified processes in trickle bed reactors, and demonstrates their versatility in application.

1. Introduction

In the field of heterogeneously catalyzed multiphase reactions trickle bed reactors (TBRs) represent a highly relevant reactor type. Common fields of application are hydrodesulfurization, hydrogenation and oxidation reactions. For the hydrodynamic description of a TBR, several phenomena need to be accounted for including flow regime, pressure drop, phase distribution, wetting of catalyst, gas–liquid (g–l) and liquid–solid (l–s) mass transfer, axial dispersion, and heat transfer. Available equations describing the hydrodynamics are often limited to a narrow process window and are valid for the type of catalyst bed used, while featuring high uncertainty due to the transient character of multiphase flow. Studies on the hydrogenation of aromatic compounds showed that g–l mass transfer, l–s mass transfer and pore diffusion often limit the reaction [1–4].

Low gas solubility in combination with slow diffusion in the liquid phase makes mass transport an important factor in the choice of catalyst and the design of TBR internals [5]. Studies showed that fast chemical reactions in combination with low gas solubility are usually limited by g–l mass transfer [1–3]. Therefore, there is a need to develop innovative catalyst structures with enhanced mass transfer characteristics. An increase in the pressure of the gas can improve the reactor performance but is resulting in higher equipment and operation costs. Therefore, the development of reactor internals leading to an intensified g–l mass transfer at low pressures seems promising. Rapid progress in the development of additive manufacturing technologies allows for the application of precisely defined geometries adapted to overcome possible process limitations in chemical reactors.

Different types of internals for TBR bring various advantages and disadvantages. The most commonly used type of packing in the chemical industry is the random packed bed, as it is simple and inexpensive to manufacture and initial catalyst loading and subsequent catalyst changes are easy to carry out.

Periodic open cellular structures (POCSs) on the other hand are an emerging class of structured catalysts which are designed by the three dimensional replication of a characteristic unit cell. POCS can be classified into strut-based and sheet-based [6,7]. These differ in the interaction of fluids with the structure with respect to hydrodynamics and pressure drop. Due to the low structure porosity, fluid interaction with strut-based POCS is low resulting in a low pressure drop. Sheet-based POCS offer the potential for increased interaction with the fluid, as

* Corresponding author.
E-mail address: hannsjoerg.freund@tu-dortmund.de (H. Freund).

https://doi.org/10.1016/j.cep.2024.109930
Received 15 May 2024; Received in revised form 28 July 2024; Accepted 3 August 2024
Available online 10 August 2024

sheets oriented horizontal to the main flow direction induce deflection of the flow.

Strut-based POCS feature low pressure drop [8], high liquid holdup [8,9] and low maldistribution [10] in multiphase reactions. At present, additive manufacturing of structured packings is limited to a few chemically, mechanically and thermally stable materials that can withstand the often harsh process conditions in the chemical industry and are expensive to produce and functionalize as catalysts. A proof of concept on the meter reactor scale has been conducted for a hydrodesulfurization process, in which the liquid distribution homogeneity was increased avoiding bypass fluxes [11]. Literature on g–l mass transfer for POCS does not appear to be available at present. In light of these findings, a general discussion is presented regarding the g–l mass transfer in random packed beds and open cellular foams. Furthermore, the transferability of these findings to POCS is investigated.

Few studies are available on investigating open cell foams structurally similar to POCS in multiphase applications. Here, studies on pressure drop and flow patterns are available for metal foams in horizontal pipes [12,13]. Gas–liquid distribution in a TBR with co-current downward flow [14] as well as flow patterns, residence time distribution, specific surface area, holdup and g–l mass transfer in co-current downward flow in milli-reactors have been investigated [15–17]. A detailed flow regime map comparing cellular foams to conventional packed beds is available in literature [18]. The transition from trickle- to pulse-flow regime with cellular foams inserted requires higher gas and liquid superficial velocity compared to packed beds [18]. The increase in the cell density of a cellular foam leads to a further elevation of the flow transition level [18].

The g–l mass transfer in random packed beds is well understood for water–air systems at moderate temperature and pressure. The g–l mass transfer correlates with the pressure drop of the packing. An increase in pressure drop results in a higher g–l mass transfer coefficient due to intensified mixing [19]. Therefore, the mass transfer coefficients in g–l mass transfer applications using strut-based POCS, e.g., cubic, Kelvin or diamond unit cell structures, are expected to be low, although the potentially improved liquid distribution yields an increase in g–l interphase area. The potential solution of this challenge is represented by the high design flexibility of POCS given by additive manufacturing. Therefore, we here propose a novel unit cell design inducing high pressure drop while maintaining other beneficial characteristics of POCS such as radial dispersion and homogeneous liquid distribution.

In this work, g–l mass transfer in a TBR using POCS was investigated for the first time and g–l mass transfer coefficients were determined experimentally using the well established desaturation method described by Goto and Smith [20]. The g–l mass transfer is influenced by the wettability of the solid by the liquid phase, but not by catalytic activity and particle porosity of an possible catalyst in a TBR [5]. Therefore, the comparison of g–l mass transfer of different internals can be made with inert material of similar wettability. For ensuring similar wettability, ABS and PC were used due to their similar surface free energy. For better comparability to literature data, random packed beds with spherical particles were used as a benchmark and strut-based Kelvin and diamond unit cell POCS are compared in terms of pressure drop and g–l mass transfer characteristics in order to identify the potential of POCS in the field of multiphase applications [8,10,11,21]. Finally, a novel sheet-based POCS unit cell design for intensified g–l mass transfer is introduced, enforcing meandering flow patterns. The functionality of the novel design is investigated as proof of concept.

2. Methods

2.1. Experimental setup

The mass transfer measurements were carried out using the established method according to Goto and Smith [20] via the degassing of atmospheric oxygen from deionized water with nitrogen in steady state. Prior to a desaturation experiment, water was saturated with air at atmospheric pressure in a storage tank. The oxygen concentration measured after saturation was used as inlet concentration during the desaturation experiment. The degassing of oxygen-saturated water is investigated with and without packing.

A scheme of the experimental setup used in this work is given in Fig. 1. The setup consists of the storage tank for presaturation and for the liquid feed, gas and liquid dosing, a bubble column for saturation of inlet gas with water and the trickle bed itself. The trickle bed was operated in co-current downward mode. The measuring section includes a transparent PVC pipe with an internal diameter of 35.2 mm and a maximum packing height of 1000 mm. The oxygen content was measured using an optical oxygen sensor, *PreSens OXYbase*, with an accuracy of ±0.1 % of the measured value, and was positioned downstream the gas–liquid separation at the reactor outlet. The oxygen sensor includes an internal temperature sensor. The pressure drop of the packing, the flow distributor and the retaining sieve was measured via the *WIKA air2guide* pressure differential transducer with an accuracy of ±1.5 % of the obtained value. Gas volume flow was regulated using a mass flow controller (*Bronkhorst Mass-Stream*), while a pump (*Gardena Gartenpumpe 3000/4*) conveyed the liquid volume flow, under manual restriction by means of a needle valve. Owing to the considerable pumping head, a part of the pumped liquid flow was recirculated back into the water storage tank, not shown in the diagram for the benefit of better readability. The flow rate was determined by a rotary flow meter (*Digmesa FHKU G1/4"*) with an accuracy of 11.6 % after calibration. Data acquisition for all sensors involved was automated using a digital transducer of the type *Delphin Technology ExpertKey 100L*. To prevent any interference with the desorption of oxygen by evaporation, the inlet gas flow was saturated with water using a bubble column with a height of 1 m. In order to avoid hysteresis effects due to initial wetting of the bed the Kan prewetting method was used [22]. After prewetting the bed at the maximum superficial liquid velocity of 0.023 $m\,s^{-1}$ for a minimum of 5 min, the desired gas and liquid fluxes were set.

An overview on the measured packings and operational parameters is given in Table 1. For each structure, gas and liquid velocity were varied. Due to the need for reliable empty bed experiments, the applied gas and liquid flow rate were limited to three distinct values. Benchmark experiments were conducted for all given operational parameter combinations. Whenever the relative difference between measurements with empty bed and with packing were small, statistical deviations led to negative pressure drop and/or mass transfer coefficients. Such experiments with negative pressure drop or negative g–l mass transfer coefficients were excluded. For random packed beds with spherical particles at high gas and liquid flow rate, the maximum pressure drop of the sensor was exceeded and therefore not considered for calculations. Experiments with spheres were repeated several times during the measurement campaign as a standard experiment to track time dependent shifts in the acquired data. Empty bed experiments were repeated at least three times to ensure reliable reference data for each operational parameter combination. Every set point in the experimental plan was reproduced at least twice. Due to flooding behavior in the gas–liquid separation occurring for Kelvin and H internals at 0.49 $m\,s^{-1}$ the maximum gas superficial velocity was reduced to 0.25 $m\,s^{-1}$ for those structures. A homogeneous initial liquid distribution was realized with a liquid distributor placed on top of the measured reactor bed. In order to check for the independence of the pressure drop and volumetric g–l mass transfer coefficient from the bed height an bed height variation was conducted with spherical packed beds and diamond unit cell structures. No such effects were identified. Therefore, a height variation for Kelvin and H structure internals was not conducted. The height of the internal structure has been set to facilitate the measurement of a global mass transfer that will result in dissolved oxygen concentrations in the range of the dissolved oxygen sensor under all conditions.

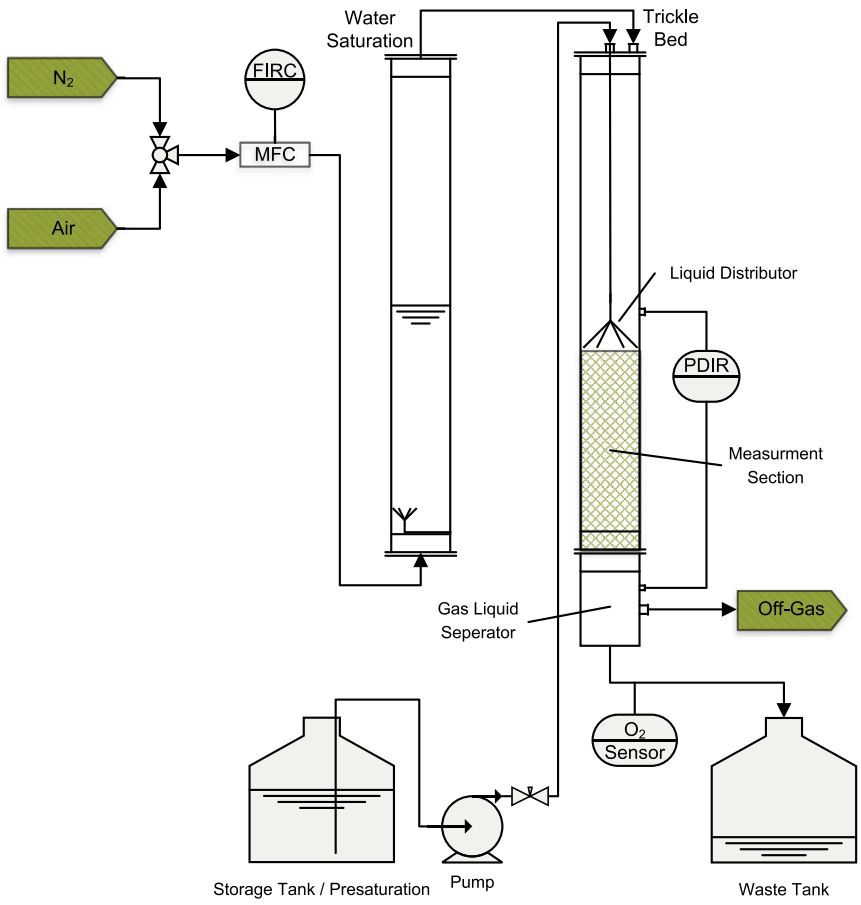

Fig. 1. Flow chart of the setup used for g–l mass transfer measurements.

Table 1
Overview of packings and operational conditions of the experiments carried out to determine pressure drop and g–l mass transfer coefficients.

	ϵ_s/ –	a/ $m^2\,m^{-3}$	L_p/ mm	u_l/ $m\,s^{-1}$	u_g / $m\,s^{-1}$
Spheres	0.26	1067	200	0.005	4 × 0.092; 3 × 0.25
				0.014	11 × 0.092; 6 × 0.25
				0.023	3 × 0.092; 3 × 0.25
			300	0.005	2 × 0.092; 3 × 0.29; 6 × 0.49
				0.014	2 × 0.092; 2 × 0.29; 2 × 0.49
				0.023	2 × 0.092; 1 × 0.29; 2 × 0.49
			500	0.005	4 × 0.092; 2 × 0.29; 2 × 0.49
				0.014	2 × 0.092
				0.023	1 × 0.092
Diamond	0.52	1422	300	0.005	2 × 0.092; 5 × 0.29; 1 × 0.49
				0.014	4 × 0.092; 1 × 0.29; 2 × 0.49
				0.023	1 × 0.092; 3 × 0.49
			500	0.005	3 × 0.49
				0.014	1 × 0.092; 3 × 0.29; 3 × 0.49
				0.023	2 × 0.29; 1 × 0.49
Kelvin	0.81	1067	300	0.005	3 × 0.25
				0.014	4 × 0.092; 6 × 0.25
				0.023	3 × 0.092; 5 × 0.25
H	0.72	647	90	0.005	2 × 0.092; 2 × 0.25
				0.014	2 × 0.092; 2 × 0.25
				0.023	2 × 0.092; 2 × 0.25
Empty	–	–	0	0.005	12 × 0.092; 5 × 0.29; 6 × 0.25; 3 × 0.49
				0.014	15 × 0.092; 6 × 0.29; 12 × 0.25; 5 × 0.49
				0.023	10 × 0.092; 4 × 0.29; 6 × 0.25; 7 × 0.49

ϵ_s: Volume fraction of solid, a: Volume specific g–l interphase, L_p: height of packed bed, u_l: Liquid superficial velocity, u_g: Gas superficial velocity, #x: Number of repetitions.

Table 2
Overview on the geometric parameters of sphere packing and POCS used for the investigation of g–l mass transfer.

Name	Geometry parameters /mm	Porosity /–	Specific surface area /$m^2\ m^{-3}$
Spheres	d: 3	0.26	1067
Diamond	a: 2.8, d_s:1	0.52	1422
Kelvin	a: 3.24, d_s: 0,62	0.81	1067
H	a: 12, b: 9.5, c: 15, d: 15, w: 1	0.72	647

Table 3
Calculation of specific surface area and porosity of Kelvin and diamond unit cell POCS based on characteristic geometric parameters.

	Kelvin	diamond
l_s:	$a \cdot \frac{\sqrt{2}}{4}$	$a \cdot \frac{\sqrt{3}}{4}$
d_w:	$\left(\frac{6\cdot\sqrt{3}}{\pi}\right)^{0.5} \cdot \left(l_{s,K} - \frac{\sqrt{3}}{3} \cdot d_s\right)$	$2 \cdot \left(\frac{6\cdot\sqrt{3}}{\pi}\right)^{0.5} \cdot \left(l_{s,D} - \frac{\sqrt{3}}{3} \cdot d_s\right)$
ϵ:	$1 - \frac{3\cdot\pi}{8\cdot\sqrt{2}\cdot\left(\frac{l_{s,K}}{d_s}\right)^3} \cdot \left(\frac{l_{s,K}}{d_s} + \frac{2-2\cdot\sqrt{2}}{3}\right)$	$1 - \frac{3\cdot\sqrt{3}\cdot\pi}{16\cdot\left(\frac{l_{s,D}}{d_s}\right)^3} \cdot \left(\frac{l_{s,D}}{d_s} + \frac{\sqrt{2}}{2}\left(\frac{1}{3} - \frac{\sqrt{3}}{2}\right)\right)$
S_v:	$\frac{3\cdot\pi}{2\cdot\sqrt{2}\left(\frac{l_{s,K}}{d_s}\right)^3 \cdot d_s} \cdot \left(\frac{l_{s,K}}{d_s} + \sqrt{2} - 2\right)$	$\frac{3\cdot\sqrt{3}\cdot\pi}{4\cdot\left(\frac{l_{s,D}}{d_s}\right)^3 d_s} \cdot \left(\frac{l_{s,D}}{d_s} + \frac{\sqrt{3}}{2} - \frac{\sqrt{2}}{2} - \frac{3}{4}\right)$

2.2. Geometrical properties of structured packings and packed beds

In the following, the structures used and manufactured for the g–l mass transfer experiments are presented. Table 2 gives an overview on the measured structures. In the following, the definitions for the geometry parameters and the calculations for porosity and volume specific surface area are presented. A summary is given in Table 3.

2.2.1. Random packed bed (spheres)

For better comparability of the conducted experiments to the literature a random packed bed consisting of massive and polished spheres made from soda-lime glass (*Marienfeld GmbH & Co. KG*) with a diameter of 3 mm was used as a benchmark. The height of the packed bed was varied to 0.2 m, 0.3 m and 0.5 m. The void fraction (porosity, ϵ_S) of the packed bed was calculated based on volume (V_b) and weight (m_G) of the glass beads in a measuring cylinder of comparable diameter to the measurement setup and the density of soda-lime glass (ρ_G).

$$\epsilon_S = \frac{m_G}{\rho_G \cdot V_b} \tag{1}$$

The volume specific surface area of the spheres ($S_{v,S}$) was calculated from the porosity and the diameter of the spheres (d_S).

$$S_{v,S} = \frac{6}{d_S} \cdot \epsilon_S \tag{2}$$

The according parameters are given in Table 2.

2.2.2. Strut-based POCS (Kelvin & diamond)

Kelvin and diamond unit cell POCS geometry can be described with the strut diameter (d_s) and the cell size (a). Both unit cells are shown in Figs. 2(a) and 2(b). Equations for calculation of the porosity (ϵ) and specific surface area (S_v) of both structures are given by Horneber [23] and are summarized in Table 3. The geometrical parameters of both structures are given in Table 2.

The POCS were manufactured with an extrusion-based fused filament fabrication (FFF) printer *Ultimaker 3S* from ABS material (*Ultimaker ABS Premium Filament*) with a 0.25 mm nozzle. Modifications of the standard building parameters were required as extensive stringing and unstable builds occurred for small strut diameters. Good printing results were achieved with brim build plate support, a maximum fan speed for cooling the filament after deposition, enabled filament retraction for moving the nozzle between isolated struts, a layer height of 0.1 mm and a printing speed of 15 mm s^{-1}. Despite adequate printing conditions, deviations between the digital and the manufactured structure remain. Due to the layer-wise building process, resulting surface roughness is higher compared to the digital structure. Other building defects such as stringing can plug the unit cell windows and therefore influence the hydrodynamics inside the structure. All strut-based POCS were produced in sections of 100 mm and stacked subsequently to achieve the overall packing height. All strut-based POCS were manufactured without an outer wall. A good wall contacting of the structure was assumed as force was necessary to insert the structures into the PVC pipe of the setup.

For better comparability, the tunable specific surface area of Kelvin unit cell POCS was adjusted to the specific surface area of the spherical particle bed. The surface of the diamond unit cell POCS was adjusted to the surface of an ideal packed bed of 3 mm spheres. The window diameter of the POCS was maximized to avoid plugging of windows during the building process.

2.2.3. Sheet-based POCS (H unit cell)

For a high g–l mass transfer a strong interaction between gas and liquid phase as well as a high g–l interface area is mandatory. According to the findings of Iliuta et al. the g–l mass transfer coefficient correlates with the liquid superficial velocity and the two phase pressure drop of a packed bed [19]. Both parameters can be increased without the change in gas and liquid volume flow within a TBR with given diameter by introducing meandering flow. Due to the necessity of the flow to pass radial or axial coordinates several times, the available cross section for the flow is drastically reduced. At the same time, the direction of liquid flow is frequently turned by 180° leading to friction and increased turbulence. In co-current downward flow, the meandering pathway can be designed starting with a 90° or a 180° turn at the inlet of the structure resulting in radial or axial orientation of flow channels.

The implementation of a radially meandering flow is assumed to lead to a separation of liquid and gas phase in the channels resulting in the formation of segregated flow and therefore in a reduction of the wetted surface on downward oriented surfaces. More promising seems the development of a structure leading to axially oriented meandering channels.

Meandering flow imposes constraints on the design of sheet-based POCS. Most obvious, but also most important, is a design that allows flow in the downward direction without forming dead ends. As fluids will favor the path of least resistance, bypasses parallel to meandering channels must be avoided. Furthermore, radial mixing must be ensured for a homogeneous liquid distribution, because channels with less liquid will promote increased gas flow, which ultimately can lead to a diversion of liquid distribution to channels solely filled with either liquid or gas.

Considering the presented constraints one can imagine some vertical oriented meandering streamlines in 2D which need to periodically contact for radial mixing. By filling the empty spaces between the streamlines with solid a structure is created enforcing meandering flow. In two dimensions this solid resembles the capital H, therefore we name this structure “H unit cell”. This H unit cell, visualized in Fig. 3, is inspired by fractal geometries in chemical engineering as proposed by Coppens et al. [24,25] for intensification of mass transfer. It can be seen that each streamline has to pass one axial level of the reactor three times. Therefore, the available effective cross-sectional area is approximately one third of the free cross section assuming a differential wall thickness. The upward and downward velocity can be individually tuned by adjusting the block width a and the cell width c resulting in a change of the cross-sectional area for upward or downward flow.

In order to reflect the behavior of the two-dimensional H, it was translated into a three-dimensional cuboid without top and bottom plane as well as a dividing plane in the center. Other base planes such as triangles, hexagons or circles are also possible, but the quadratic plane is the most easiest one to construct and calculate. The horizontal positioning of the cuboids is arranged in the form of a net, where the knots are representing the center of the cuboid. For mixing of

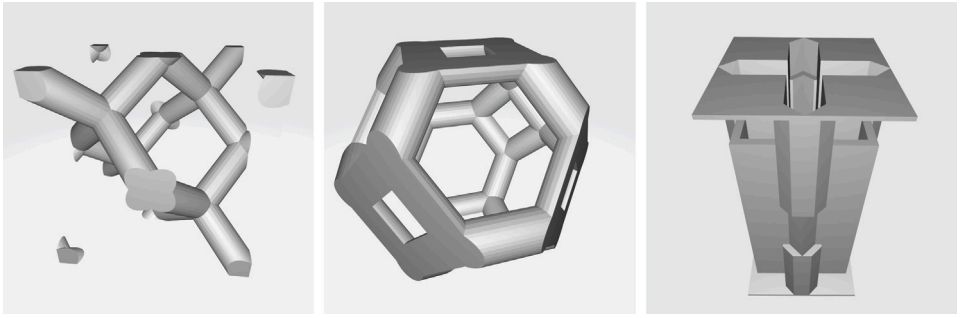

(a) CAD: Diamond unit cell (b) CAD: Kelvin unit cell (c) CAD: H unit cell

Fig. 2. Unit cells of the three POCS applied in this work.

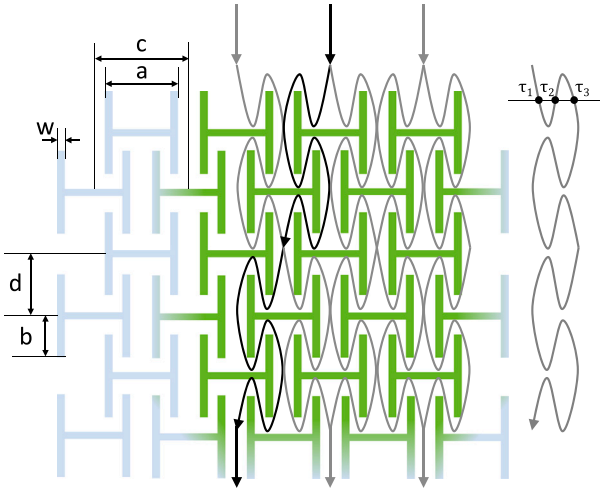

Fig. 3. Two dimensional visualization of axial meandering flow with an H-structure. a: block width, b: block height, c: cell width, d: cell height, w: wall thickness, τ: indication for different residence times at one axial height.

fluid in width and depth, one block has to overlap with four blocks below. Therefore, the upper layer is moved half of the cell width c in width and depth direction, respectively. However, this arrangement leads to formation of a bypass channel as shown in Fig. 4 (left). For closing the potential bypass channel, the quadratic base layer of a three-dimensional H-block is adapted to a star shape. Each spike covers exactly one quarter of the formed bypass channel. The resulting star shape and positioning is displayed in Fig. 4 (right). A CAD drawing of the unit cell is given in Fig. 2(c). The proposed H unit cell can be described by two parameters for the block (block width a and block height b) together with the two parameters for stacking (cell width c and cell height d) as well as the wall thickness w. The resulting structure appears to diverge from the established norms of reactor internals, rendering a comparison to other internals untenable.

Due to the novelty of the structure, equations for the calculation of porosity and specific surface had to be developed. The derivations are given in the supplemental material. Furthermore, an stl-file of a representative unit cell as well as cross sections are given for better understanding of the geometry of the structure. The structure can be divided into three characteristic sections — channel section, deflection section and H-bar (Fig. 5(a)) — fulfilling different functions. The channel section allows fluids to flow up and down in parallel. The downward channels are cross-shaped, while the upward channels are rectangular. In the deflection section, the flow is deflected by 180° and flows from an upward flow rectangle to a downward flow cross and vice versa. In each deflection section, four fluxes from different H-blocks come into contact allowing for fluid exchange in the radial direction along the axial coordinate. The H-bar on the one hand allows the fluid to pass from one level to the next and on the other hand forms the physical barrier required for the operation of the deflection zones.

For the manufacturing of the H unit cell the same additive manufacturing device as for the strut-based POCS was used. In order to make the flow inside of the structure visible, transparent PETG filament (*Ultimaker PETG Filament*) was used. The structure was printed in the direction of the intended flow. Therefore, all areas orthogonal to the main flow direction need to be supported during the building process. As support material water soluble PVA Filament (*Ultimaker PVA Premium Filament*) was used in dual extrusion mode. The PVA was later removed by purging the structure with hot water for several hours, until no foaming of water was observable, which indicated the complete removal of the PVA. The necessity to flush the structure after printing limited the minimal cell size. Plugging of channels by stringing or other building effects must be avoided at all time. Therefore, a specific surface area equal to that of a spherical packed bed could not be achieved. Therefore, the H unit cell POCS was designed with approximately same areas for upward and downward flow as well as smallest possible combination of b and d, determining the dimensions of the quadratic channels, with upward oriented flow. A wall thickness of 1 mm was chosen for mechanical stability. An aspect ratio of 1:2 was chosen for width:height ratio of the unit cell to introduce frequent 180° turns and keep characteristics of a channel between the turns. To avoid bypass flux between the wall of the pipe and the structure, the structure was printed with an outer wall of the thickness w. Furthermore, a disk at the bottom of the structure was printed which was sealed between the flange at the bottom of the test plant replacing the sieve used for all other types of packing. With this construction the fluids were forced to run through the H-structure and a bypassing was avoided.

2.3. Pressure drop correlation

The measurement of two-phase pressure drop in a TBR gives information on the flow regime as well as on the g–l mass transfer. Moreover, the pressure drop itself is an important design parameter for a TBR. Many correlations for the estimation of pressure drop in random packed beds are available and reviewed elsewhere [5]. To prove validity of the data generated by the experimental plant, the measured pressure drop was compared to the pressure drop predicted with a state-of-the-art data-driven neural network approach of Iliuta et al. [26], that is based on the extended Holub model [27]. This model is applicable in trickle flow regime and is trained on over 4000 experiments from 65 references. Required thermophysical properties such as viscosity, density and surface tension were taken from literature [28].

Transferring this model to POCS is not feasible, because their porosity exceeds the range of applicability of the model. Furthermore, a characteristic length, required for dimensionless description of the geometry, is not clearly defined for POCS yet [7] and the applied neural network is not trained on POCS geometries. Therefore, the preceding

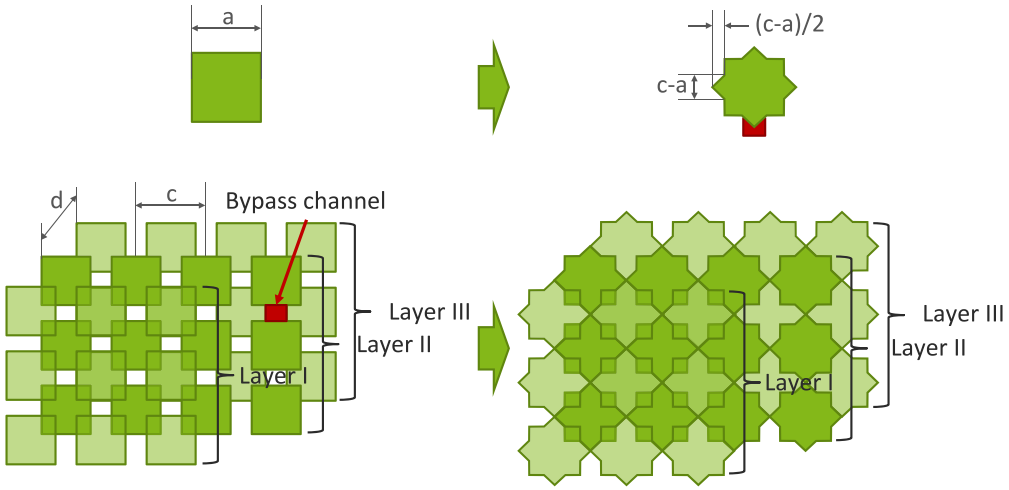

Fig. 4. Stacking of H build cuboids (left) and H star shape (right) in top view. Red square highlights the formation of bypass channels.

experiments with established POCS are compared to the model of Lämmermann et al. [10] developed for the Kelvin, diamond and DiaKel (hybrid unit cell combining the diamond and Kelvin unit cell) POCS. The model is based on the concept of relative permeability [29,30]. The static holdup is estimated based on Eötvös correlations for the materials ABS, Ti6Al4V and stereolithographic resin. Equations for the correlation of the two-phase pressure drop of the novel H unit cell POCS were not developed due to the need for liquid holdup measurements, which were not performed in this work.

2.4. Gas–liquid mass transfer coefficients

The volumetric g–l mass transfer coefficient of a packing can be calculated from the difference between empty pipe mass transfer and mass transfer with packing [20]. Because the inlet concentration was not always at full saturation with oxygen, the literature equation was adjusted by solving the mass balance for oxygen in the system.

$$k_l a = \frac{\dot{V}_l}{A_R \cdot L_p} \cdot \ln\left(\frac{\left(\frac{c_{O_{2,l,out,empty}}}{c_{O_{2,l,out}}}\right)}{\left(\frac{c_{O_{2,l,in,empty}}}{c_{O_{2,l,in}}}\right)}\right) \tag{3}$$

Fig. 6 illustrates the measurement procedure. The inlet concentration was determined after completion of the saturation process. It was assumed that all liquid in the storage tank had the same concentration. The determination of the steady-state outlet concentration, an exponential function given in Eq. (4), was fitted to the experimental data after switching to desaturation.

$$c_{O_{2,out}} = x_1 - x_2 \cdot \exp(-x_3 \cdot t) \tag{4}$$

The parameter estimation for each experiment was conducted with the function *optimize.curve_fit* of the *python* module *scipy*. The exponential function resembles the data and the steady-state outlet concentration is given by the parameter x_1. The empty bed inlet and outlet concentrations were averaged for the calculation of $k_l a$ values of each desaturation experiment with packing. The $k_l a$ values of each experiment were averaged for same operational conditions and packing type. The statistical deviation of measured concentrations was considered with Gaussian error propagation for the calculation of $k_l a$ values. Small differences between the empty bed outlet concentration and the outlet concentration with a bed result in a high uncertainty of the determined $k_l a$ values. Therefore, experiments with an overall mass transfer approximately below $0.011\,s^{-1}$ are neglected. For the applied random packed bed the liquid-side mass transfer coefficient was estimated with the model of Larachi et al. [31] for a representative bed height of 300 mm. Necessary diffusion coefficients for oxygen in water were taken from literature [32]. The estimated values enable a comparison of the measured mass transfer coefficients to literature results used to train the applied neural network.

3. Results

In the following, the results on pressure drop of the four different packings (spheres, diamond, Kelvin, H unit cell) are presented and compared to literature correlations. Furthermore, the g–l mass transfer performance achieved with POCS is compared to the results of the sphere benchmark. The achieved integral mass transfer is qualitatively correlated to the pressure drop in the packing. Finally, the theoretical thoughts on the H unit cell POCS regarding mass transfer identification introduced by meandering flow are assessed.

The measured height specific pressure drop of the sphere packed bed and diamond POCS packing and the measured mass transfer coefficient showed no systematic deviation while varying the height of the packings. For packings with low volumetric mass transfer coefficients the height of the packing was increased. This leads to an increase in the difference between empty bed mass transfer and mass transfer with packing and consequently to a decreased error in measured mass transfer coefficients based on the mentioned Gaussian error propagation.

The overall height specific pressure drop and its fluctuations over time is indicating that most of the experiments were conducted in trickle flow regime. For sphere packed beds, the high interaction regime was likely approached at maximum liquid superficial velocities. Diamond POCS packings at maximum gas and liquid superficial velocity were likely operated in high interaction regime, indicated by a sudden increase in g–l mass transfer coefficient. The elevation of the transition from trickle to pulse flow regime to higher gas and liquid velocity is also reported for periodical open foams, which have similar characteristics as POCS with respect to pressure drop [18]. The identification and classification of flow regimes inside of the novel H unit cell POCS remains unknown.

3.1. Pressure drop

The averaged specific pressure drop of the different packings measured at different liquid superficial velocity as a function of the gas superficial velocities is displayed in Fig. 7. Furthermore, the corresponding pressure drop calculated based on presented correlations for spherical packed beds, Kelvin POCS packings and diamond POCS packings is shown. For high values of the liquid velocity, the range of

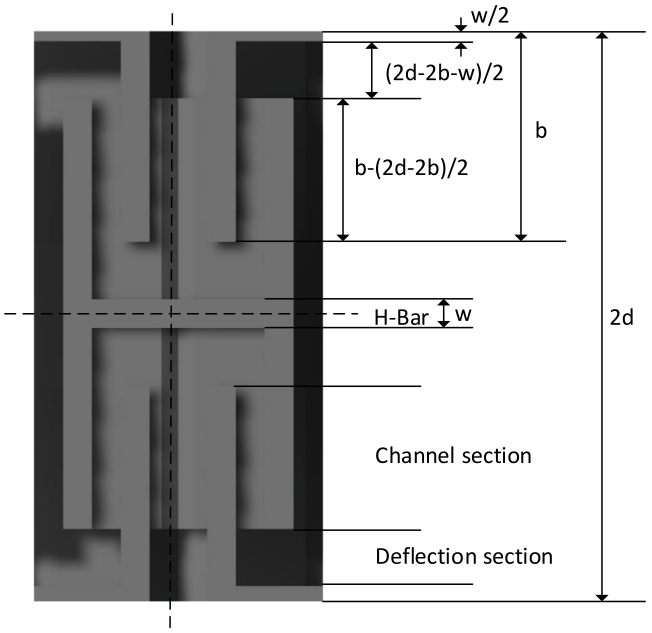

(a) Front cut view at 1/4 of cell width c

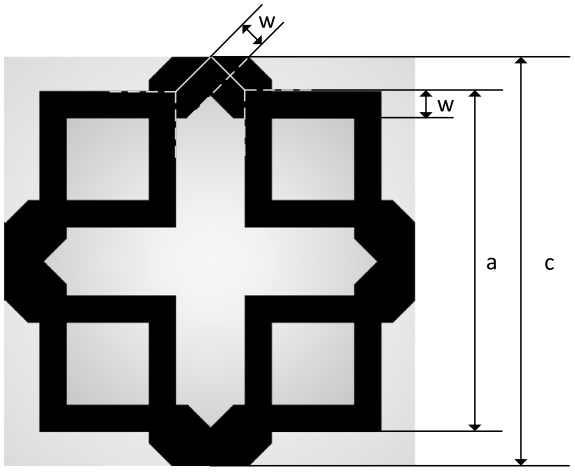

(b) Top cut view in channel section

Fig. 5. H cell dimensions and height partitions for calculation of porosity and surface area.

applicability of the applied neural network correlation for the sphere packed bed was exceeded and therefore not calculated.

As expected from literature results, the pressure drop of the benchmark sphere packed bed increases with increasing gas and liquid superficial velocity [5]. For low liquid flow rates, the correlation from Iliuta et al. [26] is in agreement with the measured pressure drop proving adequate functionality of the used experimental setup. The discontinuity of the estimation results at a liquid velocity of $0.014\,\mathrm{m\,s^{-1}}$ and a gas velocity of approx. $0.12\,\mathrm{m\,s^{-1}}$ in Fig. 7(b) is attributed either to solver settings in the iterative solution procedure or to the training dataset of the applied neural network correlation. The unexpectedly low pressure drop at medium liquid flux and high gas flux is presumed as measurement error. Measurements with 0.5 m bed length exceeded the maximum measurable pressure difference of $24\,000\,\mathrm{Pa\,m^{-1}}$, which is close to the estimated pressure drop.

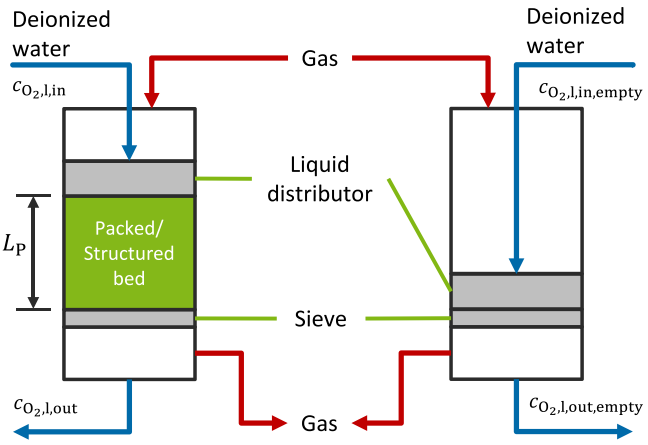

Fig. 6. Schematic diagram for the determination of g–l mass transfer coefficients. *Source:* Adapted from [20].

Compared to the benchmark experiments, strut-based Kelvin and diamond unit cell POCS packings show a significantly lower pressure drop. In general, the measured pressure drop is in the same order of magnitude as predicted values by the correlation of Lämmermann et al. [8]. The values deviate more than the reported mean average percentage error of 39.7 %. While the setup of Lämmemann et al. is comparable to the setup of this work, some differences, e.g. the use of a later version of the manufacturing unit (*Ultimaker 2+ vs 3S*), slightly bigger column diameter (30 mm and 32.5 mm) or the fact that the setup was not the same as in the work of Lämmermann et al. may be possible explanations for the deviations.

Kelvin unit cell POCS packings were within strut diameter and cell size range of the referenced work. Therefore, the correlation of Lämmermann et al. is applicable. However, while the correlation of Lämmermann et al. can describe the rise in pressure drop with increasing gas and liquid velocity, the pressure drop of Kelvin unit cell POCS is systematically overestimated in minimum by a factor of 2. Diamond POCS packings were out of range, but close to the applied structures of the reference with approx. 20 % increased strut diameter and approx. 15 % reduced cell size, resulting in approx. 40 % increased specific surface area of the maximum measured structure of the reference. Therefore, the diamond unit cell POCS packings are not in range of the correlation. However, half of the measured pressure drop data is predicted satisfactorily in trend as well as in absolute values. Pressure drop data which are not properly predicted by the correlation are generally underestimated by the correlation.

Tomographic measurement results of Littwin et al. [21] for the liquid holdup showed that local accumulation of liquid between POCS sections and between structure and tube wall can occur. The diameter of the structures for the tomographic measurements was 100 mm and therefore not directly comparable with the packings of this work. As the wall surface compared to the packing volume is higher for smaller diameters, wall effects are assumed to have a higher influence in the experimental setup used in this work. This and the characteristic transient behavior of multiphase flow in TBRs are potential explanations for the deviation of the data from the literature correlation. The comparison in Fig. 7 shows that two-phase pressure drop in POCS is not fully understood yet and demonstrates the limited applicability of available literature correlations.

The pressure drop of the novel sheet-based H unit cell POCS packing is the highest for all process conditions. Especially at low gas velocity the pressure drop in the novel H packing exceeds the pressure drop of the benchmark 1.5 to 2-fold. This confirms the functionality of the developed structure regarding the increase in pressure drop caused by deflection of the flow and by the increase in the velocity due to meandering channels. The gas and liquid upward flow in the channel sections

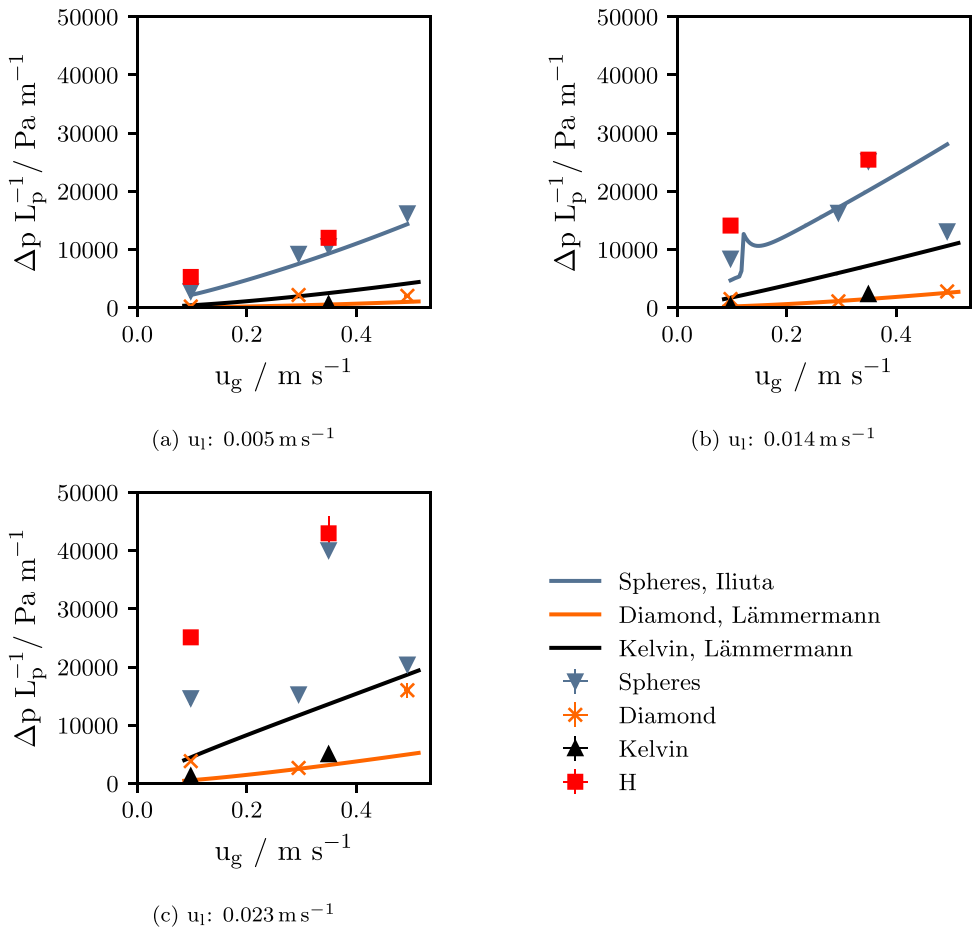

Fig. 7. Results of measured pressure drop for different packings over gas superficial velocity compared to calculated pressure drop based on literature correlations for different liquid fluxes.

of the H unit cell POCS does not allow trickle flow in these channels. As the structure was manufactured from transparent PETG filament the resulting H unit cell POCS packing is opaque. By visual analysis using backlight a flow behavior similar to slug flow was identified as gas and liquid alternate in the channels over time. Some accumulation of liquid in the deflection zones where downward to upward flow is taking place was observed. As a result, no continuous gas or liquid phase is present overall in the H unit cell structure. The continuous pattern of alternating gas and liquid zones may have a positive effect on gravity driven flux. However, this effect was not observed for the investigated packing height of 90 mm, but is assumed to have a significant influence for increased packing heights. Stagnant gas, stagnant liquid or the formation of bypass streams were not observed. The sealing concept of the structure with an integrated wall as well as with the disk in the flange were successful.

3.2. Gas–liquid mass transfer

From the correlation of Iliuta et al. [19] for random packed beds a high g–l mass transfer coefficient is expected at a high pressure drop, low liquid holdup ($\epsilon_{l,d}$) and high liquid superficial velocity.

$$k_l a = 0.0036 \cdot \left(\frac{u_l}{\epsilon_{l,d}} \cdot \frac{\Delta P}{L_p} \right)^{0.35} \tag{5}$$

Considering the continuity equation, the fraction of superficial velocity and dynamic liquid holdup resembles the average liquid velocity. Based on the pressure drop results, a high g–l mass transfer coefficient is expected for the sphere packing. Although Eq. (5) was determined with measurements in random packed beds, the assumption of increased g–l mass transfer coefficients caused from increased pressure drop seems reasonable for POCS. Therefore, the g–l mass transfer coefficient of the H unit cell POCS packing is expected to be higher than the one of the sphere packed bed. However, the average liquid velocity in the H unit cell POCS packing is approximately three times higher in the channel section, due to meandering flow. The averaged volumetric g–l mass transfer coefficients measured are displayed in Fig. 8.

For the slowest measured gas velocity, the calculated mass transfer coefficients for the random packed bed of spheres via neural network correlations from Larachi et al. [31] are in good agreement with the measured data. At medium and higher gas superficial velocity the mass transfer is underestimated by the correlation. This might be caused by the relatively large distance between the end of the packings and the dissolved oxygen sensor. Although the influence of this section should be properly considered by the empty bed mass transfer, the presence of the internals itself can influence the flow behavior downstream the packed bed. This influence seems to be more pronounced at high gas velocities in the experimental setup. This effect should influence the POCS packings as well, but cannot be validated by literature as the g–l mass transfer in POCS packings is investigated for the first time.

As expected from the low pressure drop of strut-based POCS, the measured mass transfer coefficient is low. Therefore, when strut-based POCS are considered for application in a TBR special attention needs to be paid to potential mass transfer limitations between gas and liquid phase. Significant differences between the two strut-based POCS were not observed, although the mass transfer coefficient of diamond unit cell POCS packings is expected to be higher based on the pressure drop results. The operation close to the lower detection limit of the plant is assumed to be a reason for this. For the measured diamond unit cell

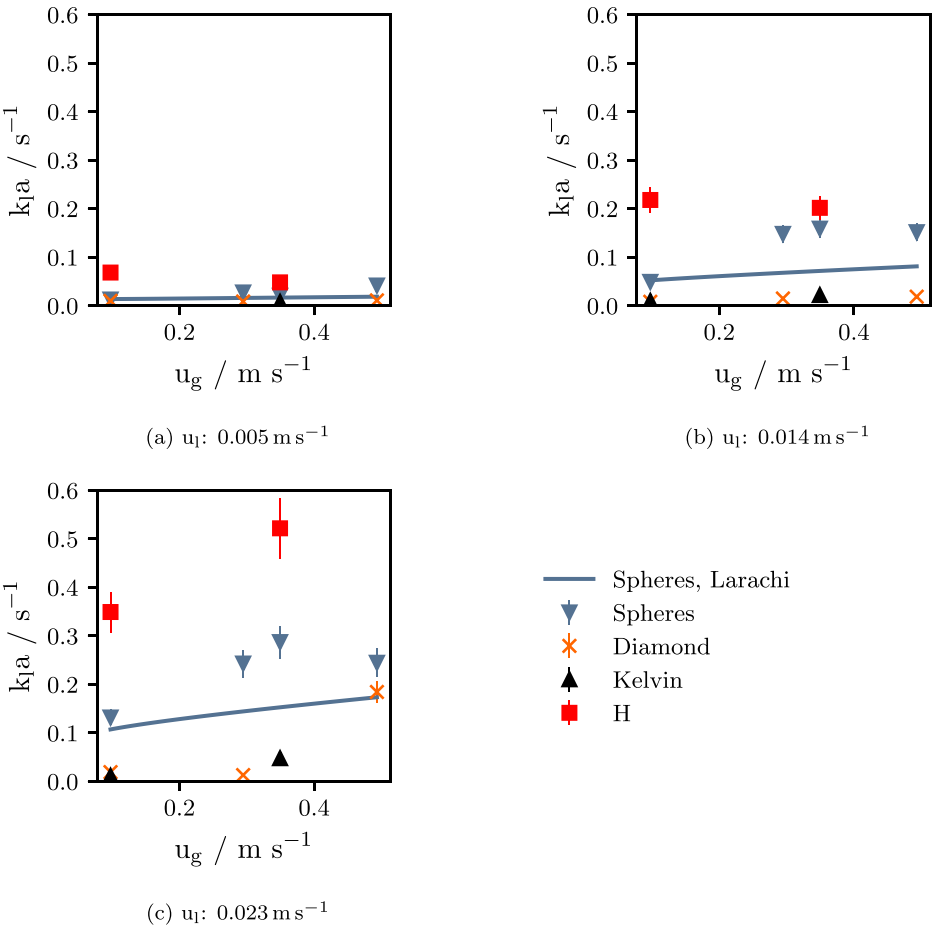

(a) u_l: 0.005 m s^{-1}

(b) u_l: 0.014 m s^{-1}

(c) u_l: 0.023 m s^{-1}

Fig. 8. Results of measured gas–liquid mass transfer coefficients ($k_l a$).

POCS packing the assumed flow regime transition at highest gas and liquid velocity is reflected in the mass transfer coefficient.

Compared to the other packings, the novel H unit cell POCS packing achieves the highest mass transfer coefficients. A clear trend to higher mass transfer rates with increased liquid velocity is given. However, for the gas superficial velocity no clear effect on the mass transfer rate is given. This can be caused by new flow regimes due to meandering flow. Deflection sections, where fluids are deflected from downward to upward flow, have to be filled with liquid to some degree preventing the formation of a continuous gas phase typical in trickle flow regime in classical TBR packings. Already at a low gas superficial velocity of 0.005 m s^{-1} $k_l a$-values from 0.07 s^{-1} to 0.37 s^{-1} can be achieved in a liquid superficial velocity range from 0.005 m s^{-1} to 0.023 m s^{-1}, respectively. In the best case at the lowest gas and liquid superficial velocity the H unit cell POCS features a factor 5 higher $k_l a$-value than the benchmark. These results underline the potential of tailor-made structures for process intensification where g–l mass transfer is a critical aspect.

3.3. Correlation of g–l mass transfer and pressure drop

TBR design is commonly based on a trade-off, as intensified mass transfer is usually paid by increased pressure drop. The evaluation of required pressure drop per achieved mass transfer is given in Fig. 9. A general trend to a higher $k_l a$-value at high pressure drop is visible. The desirable regime for a high mass transfer at low costs in terms of pressure drop can be found for a high slope between a data point and the origin of the diagram. The H unit cell POCS packing and the sphere packed bed achieved the highest mass transfer rates, while the H unit cell POCS packing achieved the maximal transfer coefficient over all experiments. Furthermore, the highest ratio of mass transfer per invested pressure drop is achieved for the H-packing within the data of reasonable accuracy. Mass transfer coefficients below approx. 0.011 s^{-1}, highlighted in red, were not considered due to the high uncertainty of the measured data. Within the investigated range of volumetric flow rate it seems that the minimum achievable pressure drop in the H unit cell POCS packing is 3- to 4-fold higher than the minimal pressure drop of the benchmark. This is presumably caused by the increase in interstitial fluid velocity due to meandering flow and the increased pressure drop in analogy to Eq. (5).

Since liquid holdup was not determined in the experiments, mass transfer coefficients could not be estimated according to Eq. (5). According to the correlation, a lower liquid velocity at the same pressure drop should result in a lower mass transfer coefficient. In average, a trend towards this behavior can be anticipated, although a sharp classification of the data points is not given.

Of course, the increase in mass transfer comes at the cost of higher pressure drop. Higher pressure drop increases both, operation costs for compressors as well as capital invest in equipment with higher pressure ratings. However, if available space is a limiting factor, the H unit cell enables the realization of more compact reactors (or separation devices) compared to the application of spherical packed beds. Packed beds with g–l mass transfer equal to the H unit cell POCS require smaller particles leading to additional challenges with homogeneous liquid distribution and packed bed fixation in the reactor.

Due to the high mass transfer rates facilitated by the H unit cell POCS in this proof of concept study the further investigations on flow regimes, liquid distribution, hold-up and heat transfer as well as additional comprehensive measurements of pressure drop and g–l mass transfer are required to generate further insights on the novel

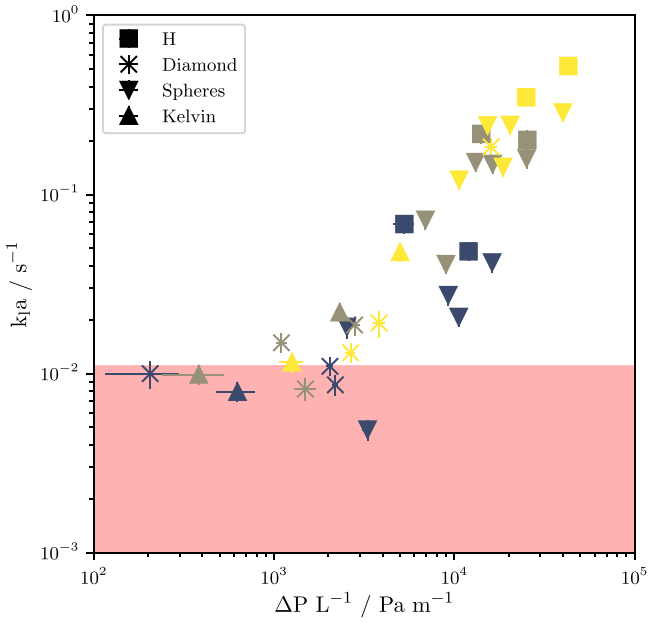

Fig. 9. Comparison of normalized pressure drop and volumetric g–l mass transfer coefficient in double logarithmic scale. Liquid superficial velocity (u_l) blue: 0.005 m s^{-1}, green: 0.014 m s^{-1}, yellow: 0.023 m s^{-1}. Red box indicates high uncertainty in measurement data.

sheet-based POCS. Regarding the manufacturing of H unit cell POCS an assembly by stacking and welding or soldering of metal base body is possible, enabling high heat conductivity in the structure as well as good mechanical stability of the structure. Moreover, modifications to the structure, such as the incorporation of tubes for thermal fluids, facilitate enhanced functionality and enables further process intensification.

4. Conclusion

In this work, pressure drop and gas–liquid mass transfer coefficients were measured for additively manufactured strut-based POCS (Kelvin and diamond unit cell), novel sheet-based POCS (H unit cell) and conventional random packed beds of spherical particles (spheres) as a benchmark. The experiments were conducted in a co-current downward flow trickle bed based on stripping experiments of water saturated with atmospheric oxygen by nitrogen at ambient pressure and temperature. The results from the benchmark experiments are in good agreement with literature correlations, which can be seen as a proof for the reliability of the measurement setup and the applied method. Pressure drop in strut-based POCS is yet not fully understood and comparability of data to existing literature correlations was shown to be limited. The presented results can be used for the development of correlations of g–l mass transfer rates with pressure drop in POCS. However, additional liquid holdup measurements are required for adequate description. The characteristic low pressure drop in strut-based POCS was confirmed and was shown to result in low overall gas–liquid mass transfer coefficients in analogy to random packed beds. Based on these results, a novel sheet-based POCS (H unit cell) was designed to generate a high pressure drop by enforcement of meandering flow patterns. A pressure drop of 45 000 Pa m^{-1} was realized resulting in a $k_l a$-value of 0.52 s^{-1} proving the concept of enforced meandering flow for mass transfer intensification. Adapting POCS for g–l mass transfer applications by changing the design of the unit cell highlights the potential of additive manufacturing for the chemical industry. Compared to the benchmark of spherical particles at low liquid and gas superficial velocity the $k_l a$-value of the H unit cell POCS packing was increased by a factor of 5. This makes the application of the novel H unit cell POCS attractive for g–l mass transfer limited reactions or absorption processes, especially in applications which require compact design.

Symbols

A_R	reactor cross sectional area in axial direction/m^2
A_i	cross sectional area in axial direction (appendix)/m^2
L_p	length of packing/m.
S_v	volume specific surface area/m−1
S_i	outer surface (appendix)/m^2
U_i	circumference in axial direction (appendix)/m.
$\dot{V}_l$	volume flux of liquid/m^3 s^{-1} .
a	unit cell size of strut-based POCS/ width of an H-block/m.
b	half height of an H-block/m.
$c_{O_2,l,in,empty}$	empty bed dissolved oxygen concentration at reactor inlet/mol m^{-3}
$c_{O_2,l,in}$	dissolved oxygen concentration at reactor inlet/mol m^{-3} .
$c_{O_2,l,out,empty}$	empty bed dissolved oxygen concentration at reactor outlet/mol m^{-3}
$c_{O_2,l,out}$	dissolved oxygen concentration at reactor outlet/mol m^{-3}
c	cell width of an H unit cell/m.
d_S	diameter of spheres/m.
d_s	strut diameter of a POCS/m.
d_w	window diameter/m.
d	half height of an H unit cell/m.
$k_l a$	volumetric gas–liquid mass transfer coefficient/s^{-1}
l_s	strut length of a POCS/m.
m_G	mass of glass spheres/kg.
t	time of the experiment/s.
u_g	gas superficial velocity/m s^{-1}
u_l	liquid superficial velocity/m s^{-1}
w	wall thickness of an H unit cell/m.
x_i	parameters for exponential fit/–.

Greek symbols

ϵ_s	volume fraction of solid/–.
ϵ	void fraction/–.
ΔP	pressure drop/Pa^{-1} .

CRediT authorship contribution statement

Hendrik Held: Writing – original draft, Visualization, Validation, Software, Methodology, Investigation, Formal analysis, Data curation, Conceptualization. **Hannsjörg Freund:** Writing – review & editing, Supervision, Resources, Methodology, Funding acquisition, Formal analysis, Conceptualization.

Declaration of competing interest

The authors declare that they have no known competing financial interests or personal relationships that could have appeared to influence the work reported in this paper.

Data availability

Data will be made available on request.

Declaration of Generative AI and AI-assisted technologies in the writing process

Statement: During the preparation of this work the authors used DeepL Write in order to improve the language and ChatGPT in order to count and limit the word number in the abstract. After using this tool/service, the authors reviewed and edited the content as needed and take full responsibility for the content of the publication.

Acknowledgments

The authors kindly acknowledge Adrian Feiler, Franziska Söhngen, Gayathri Venkatharathnam and Nils Kolberg for their commissioning of the experimental plant, the conduction of measurements and the additive manufacturing of POCS.

Appendix A. Calculation of volumetric surface area and porosity of the novel H unit cell

The H unit cell can be organized into three sections, displayed in Fig. 5(a). The first one is the channel section, which can be described by crosses and squares according to Fig. 5(b). The flow direction in the crosses is downward and upwards in the squares. The crosses can be described by a quarter section of the cross due to symmetry. This quarter consists of two rectangles, a square in the center and two triangles at the outside. Therefore the area of a cross is given by:

$$A_{cross,chan.} = 4 \cdot A_{cross,square} + 8 \cdot A_{cross,chan.,rect.} + 8 \cdot A_{cross,chan.,tri.} \tag{A.1}$$

$$A_{cross,square} = (0.5 \cdot (c-a))^2 \tag{A.2}$$

$$A_{cross,chan.,rect.} = 0.5 \cdot (c-a) \cdot (a - 0.5 \cdot c - w) \tag{A.3}$$

$$A_{cross,chan.,tri.} = 0.25 \cdot (0.5 \cdot (c-a) - \sqrt{2} \cdot w) \cdot (c - a - 2 \cdot w) \tag{A.4}$$

The area of the four squares is given by:

$$A_{square} = 4 \cdot (a - 0.5 \cdot c - 2 \cdot w)^2 \tag{A.5}$$

In the deflection section the structure consists of a star area, where the actual deflection takes place, and a cross area, which guides the fluids from one layer to the subsequent one. The star area is given by eight triangles already described above and a square.

$$A_{star} = A_{star,square} + 8 \cdot A_{cross,chan.,tri.} \tag{A.6}$$

$$A_{star,square} = (a - 2 \cdot w)^2 \tag{A.7}$$

The cross area in the deflection section is slightly bigger than the cross area in the channel zone, as only half of the spikes blocking the channel formation are present.

$$A_{cross,defl.} = 4 \cdot A_{cross,square} + 8 \cdot A_{cross,defl.,rect.} + 8 \cdot A_{cross,defl.,tri.} \tag{A.8}$$

$$A_{cross,defl.,rect.} = 0.5 \cdot (c-a) \cdot (a - 0.5 \cdot c) \tag{A.9}$$

$$A_{cross,defl.,tri.} = 0.125 \cdot (c-a)^2 \tag{A.10}$$

In the H-bar section of the structure, the void cross section is given by a deflection section cross area.

$$A_{cross,defl.} = A_{cross,H\,Bar} \tag{A.11}$$

Subsequently, the wall areas are given by the difference of the void area and the base area of the unit cell.

$$A_{wall,chan.} = c^2 - 2 \cdot A_{cross,chan.} - A_{square} \tag{A.12}$$

$$A_{wall,defl.} = c^2 - A_{star} - A_{cross,defl.} \tag{A.13}$$

$$A_{wall,H\,Bar} = c^2 - A_{cross,defl.} \tag{A.14}$$

The overall length of each section in a unit cell can be calculated according to Fig. 5(a) with two channel, four deflection and two H-bar sections.

$$l_{chan.} = 2 \cdot (2 \cdot b - d) \tag{A.15}$$

$$l_{defl.} = 4 \cdot (d - b - 0.5 \cdot w) \tag{A.16}$$

$$l_{H\,Bar} = 2 \cdot w \tag{A.17}$$

The porosity of the H-structure (ϵ_H) can be calculated based on the volume of the unit cell and the volume of the solid.

$$\epsilon_H = \left. \frac{2 \cdot c^2 \cdot d - \sum_i \left(l_i \cdot A_{wall,i}\right)}{2 \cdot c^2 \cdot d} \right| i \in [chan., defl., H\,Bar] \tag{A.18}$$

For the calculation of the volume specific surface area of the structure, surfaces parallel to the main direction of flow and the surface orthogonal to the main flow direction will be considered separately. The surface area is dependent on the different sections of the unit cell. The surface in parallel to flow direction is given by the product of the circumferences times the height of the section.

$$\begin{aligned} S_{\parallel} =& (4 \cdot U_{square} + 2 \cdot U_{cross,chan.}) \cdot l_{chan.} + (U_{star} + U_{cross,defl.}) \cdot l_{defl.} \\ &+ U_{cross,H\,Bar} \cdot l_{H\,Bar} \end{aligned} \tag{A.19}$$

The surfaces can be calculated according to the definitions in Fig. 5.

$$\begin{aligned} U_{cross,chan.} =& 8 \cdot (a - 0.5 \cdot c - w + \\ & \sqrt{(0.5 \cdot (c-a) - \sqrt{2} \cdot w)^2 + (c - a - 2 \cdot w)^2} + 2 \cdot w) \end{aligned} \tag{A.20}$$

$$U_{square} = 4 \cdot (a - 0.5 \cdot c - 2 \cdot w) \tag{A.21}$$

$$U_{star} = 4 \cdot \left(2 \cdot a - c + 2 \cdot \sqrt{(0.5 \cdot (c-a) - \sqrt{2} \cdot w)^2 + (c - a - 2 \cdot w)^2}\right) \tag{A.22}$$

$$U_{cross,defl.} = U_{cross,H\,Bar} = 4 \cdot (2 \cdot a - c + \sqrt{2} \cdot (c-a)) \tag{A.23}$$

The surfaces orthogonal to the main flow direction are at the interfaces between H-bar and deflection as well as deflection and channel section.

$$S_{\perp} = 4 \cdot A_{defl.,H\,Bar} + 4 \cdot A_{chan.,defl} \tag{A.24}$$

$$A_{defl.,H\,Bar} = A_{star} \tag{A.25}$$

$$A_{chan.,defl.} = 4 \cdot (w^2 + 2 \cdot w \cdot (a - 0.5 \cdot c - 2 \cdot w)) \tag{A.26}$$

Therefore, the volume specific surface area is given by the sum of all orthogonal and parallel surfaces per volume of the unit cell.

$$S_{v,H} = \frac{S_{\parallel} + S_{\perp}}{2 \cdot c^2 \cdot d} \tag{A.27}$$

Appendix B. Supplementary data

Supplementary material related to this article can be found online at https://doi.org/10.1016/j.cep.2024.109930.

References

[1] S. Toppinen, T.-K. Rantakylä, T. Salmi, J. Aittamaa, Kinetics of the liquid-phase hydrogenation of benzene and some monosubstituted alkylbenzenes over a nickel catalyst, Ind. Eng. Chem. Res. 35 (6) (1996) 1824–1833, http://dx.doi.org/10.1021/ie9504314.

[2] C. Julcour, R. Chaudhari, J. Le Lann, A. Wilhelm, H. Delmas, Dynamic modeling of three-phase upflow fixed-bed reactor including pore diffusion, Chem. Eng. Process.: Process Intensif. 41 (4) (2002) 311–320, http://dx.doi.org/10.1016/S0255-2701(01)00147-7.

[3] J. Roininen, V. Alopaeus, S. Toppinen, J. Aittamaa, Modeling and simulation of an industrial trickle-bed reactor for benzene hydrogenation: model validation against plant data, Ind. Eng. Chem. Res. 48 (4) (2009) 1866–1872, http://dx.doi.org/10.1021/ie801411n.

[4] H. Held, H. Freund, Identification of mass transfer limitations by kinetic modeling of a technical scale trickle bed reactor for the hydrogenation of viscous aromatics, Ind. Eng. Chem. Res. (2023) http://dx.doi.org/10.1021/acs.iecr.3c03273.

[5] V.V. Ranade, R. Chaudhari, P.R. Gunjal, Trickle Bed Reactors: Reactor Engineering & Applications, first ed., Elsevier, Amsterdam, 2011.

[6] M. Benedetti, A. Du Plessis, R.O. Ritchie, M. Dallago, N. Razavi, F. Berto, Architected cellular materials: A review on their mechanical properties towards fatigue-tolerant design and fabrication, Mater. Sci. Eng. R 144 (2021) 100606, http://dx.doi.org/10.1016/j.mser.2021.100606.

[7] L. Eckendörfer, D. Rudolf, A. Brix, M. Börnhorst, H. Freund, Periodic open cellular structures in chemical engineering: application in catalysis and separation processes, Annu. Rev. Chem. Biomol. Eng. 15 (2024) http://dx.doi.org/10.1146/annurev-chembioeng-101121-085630.

[8] M. Lämmermann, G. Horak, W. Schwieger, H. Freund, Periodic open cellular structures (POCS) for intensification of multiphase reactors: Liquid holdup and two-phase pressure drop, Chem. Eng. Process. - Process Intensif. 126 (2018) 178–189, http://dx.doi.org/10.1016/j.cep.2018.02.027.

[9] G. Littwin, S. Röder, H. Freund, Systematic experimental investigations and modeling of the heat transfer in additively manufactured periodic open cellular structures with diamond unit cell, Ind. Eng. Chem. Res. 60 (18) (2021) 6753–6766, http://dx.doi.org/10.1021/acs.iecr.0c06210.

[10] M. Lämmermann, W. Schwieger, H. Freund, Experimental investigation of gas-liquid distribution in periodic open cellular structures as potential catalyst supports, Catal. Today 273 (2016) 161–171, http://dx.doi.org/10.1016/j.cattod.2016.02.049.

[11] M. von Beyer, Hydrodynamische charakterisierung der mehrphasenströmung in additiv gefertigten periodisch offenzelligen strukturen: Optionen zur prozessintensivierung in einer hydrodesulfurierungsanlage (Ph.D. dissertation), Friedrich-Alexander-Universität Erlangen-Nürnberg (FAU), 2019.

[12] R. Dyga, M. Płaczek, Influence of hydrodynamic conditions on the type and area of occurrence of gas–liquid flow patterns in the flow through open–cell foams, Materials 13 (15) (2020) 3254, http://dx.doi.org/10.3390/ma13153254.

[13] R. Dyga, S. Brol, Pressure drops in two-phase gas–liquid flow through channels filled with open-cell metal foams, Energies 14 (9) (2021) 2419, http://dx.doi.org/10.3390/en14092419.

[14] I. Mohammed, T. Bauer, M. Schubert, R. Lange, Gas–liquid distribution in tubular reactors with solid foam packings, Chem. Eng. Process.: Process Intensif. 88 (2015) 10–18, http://dx.doi.org/10.1016/j.cep.2014.11.016.

[15] J.-N. Tourvieille, R. Philippe, C. de Bellefon, Milli-channel with metal foams under an applied gas–liquid periodic flow: Flow patterns, residence time distribution and pulsing properties, Chem. Eng. Sci. 126 (2015) 406–426, http://dx.doi.org/10.1016/j.ces.2014.11.059.

[16] R.R. Zapico, P. Marín, F.V. Díez, S. Ordóñez, Liquid hold-up and gas–liquid mass transfer in an alumina open-cell foam, Chem. Eng. Sci. 143 (2016) 297–304, http://dx.doi.org/10.1016/j.ces.2016.01.008.

[17] S. Voltolina, P. Marín, F.V. Díez, S. Ordóñez, Open-cell foams as beds in multiphase reactors: Residence time distribution and mass transfer, Chem. Eng. J. 316 (2017) 323–331, http://dx.doi.org/10.1016/j.cej.2017.01.113.

[18] J. Zalucky, F. Möller, M. Schubert, U. Hampel, Flow regime transition in open-cell solid foam packed reactors: adaption of the relative permeability concept and experimental validation, Ind. Eng. Chem. Res. 54 (40) (2015) 9708–9721, http://dx.doi.org/10.1021/acs.iecr.5b02233.

[19] I. Iliuta, F.C. Thyrion, Gas–Liquid mass transfer in fixed beds with two–phase cocurrent downflow: Gas/newtonian and non–newtonian liquid systems, Chem. Eng. Technol. 20 (8) (1997) 538–549, http://dx.doi.org/10.1002/ceat.270200805.

[20] S. Goto, J.M. Smith, Trickle-bed reactor performance. Part I. Holdup and mass transfer effects, AIChE J. 21 (4) (1975) 706–713, http://dx.doi.org/10.1002/aic.690210410.

[21] G. Littwin, M. von Beyer, H. Freund, Detailed investigation of liquid distribution and holdup in periodic open cellular structures using computed tomography, Chem. Eng. Process. - Process Intensif. 168 (2021) 108579, http://dx.doi.org/10.1016/j.cep.2021.108579.

[22] K.-M. Kan, P.F. Greenfield, Multiple hydrodynamic states in cocurrent two-phase downflow through packed beds, Ind. Eng. Chem. Process Des. Dev. 17 (4) (1978) 482–485, http://dx.doi.org/10.1021/i260068a016.

[23] T.J. Horneber, Thermo-fluid Dynamic Characterization and Technical Optimization of Structured Open-Cell Metal Foams by Means of Numerical Simulation (Ph.D. dissertation), FAU Erlangen-Nürnberg, 2015.

[24] M.-O. Coppens, G.F. Froment, Catalyst design accounting for the fractal surface morphology, Chem. Eng. J. Biochem. Eng. J. 64 (1) (1996) 69–76, http://dx.doi.org/10.1016/S0923-0467(96)03105-3.

[25] S. Jiang, M.-O. Coppens, J. Wang, Intensification of liquid mixing and local turbulence using a fractal injector with staggered conformation, Chem. Eng. Process. - Process Intensif. 180 (2022) 109042, http://dx.doi.org/10.1016/j.cep.2022.109042.

[26] I. Iliuta, F. Larachi, B.P.A. Grandjean, Pressure drop and liquid holdup in trickle flow reactors: improved ergun constants and slip correlations for the slit model, Ind. Eng. Chem. Res. 37 (12) (1998) 4542–4550, http://dx.doi.org/10.1021/ie980394r.

[27] R.A. Holub, M.P. Duduković, P.A. Ramachandran, Pressure drop, liquid holdup, and flow regime transition in trickle flow, AIChE J. 39 (2) (1993) 302–321, http://dx.doi.org/10.1002/aic.690390211.

[28] VDI, VDI-Wärmeatlas, Springer Berlin Heidelberg, 2013.

[29] A.E. Saez, Hydrodynamics and Lateral Thermal Dispersion for Gas-Liquid Cocurrent Flow in Packed Beds (Holdup, Permeability, Meniscus) (Ph.D. dissertation), University of California, 1984.

[30] A.E. Saez, R.G. Carbonell, A.E. Sáez, Hydrodynamic parameters for gas–liquid cocurrent flow in packed beds, AIChE J. 31 (1) (1985) 52–62, http://dx.doi.org/10.1002/aic.690310105.

[31] F. Larachi, L. Belfares, I. Iliuta, B.P.A. Grandjean, Heat and mass transfer in cocurrent gas–liquid packed beds. Analysis, recommendations, and new correlations, Ind. Eng. Chem. Res. 42 (1) (2003) 222–242, http://dx.doi.org/10.1021/ie020416g.

[32] R.T. Ferrell, D.M. Himmelblau, Diffusion coefficients of nitrogen and oxygen in water, J. Chem. Eng. Data 12 (1) (1967) 111–115, http://dx.doi.org/10.1021/je60032a036.